Global catalog of earthquake rupture velocities shows anticorrelation between stress drop and rupture velocity

Agnès Chounet[a,*], Martin Vallée[a], Mathieu Causse[b], Françoise Courboulex[c]

[a] Institut de Physique du Globe de Paris, Sorbonne Paris Cité, Université Paris Diderot, CNRS, Paris, France
[b] Université Grenoble Alpes, IFSTTAR, CNRS, IRD, ISTerre, Grenoble 38000, France
[c] Université Côte d'Azur, CNRS, Observatoire de la Côte d'Azur, IRD, Géoazur, Valbonne, France

ARTICLE INFO

ABSTRACT

Application of the SCARDEC method provides the apparent source time functions together with seismic moment, depth, and focal mechanism, for most of the recent earthquakes with magnitude larger than 5.6–6. Using this large dataset, we have developed a method to systematically invert for the rupture direction and average rupture velocity V_r, when unilateral rupture propagation dominates. The approach is applied to all the shallow ($z < 120$ km) earthquakes of the catalog over the 1992–2015 time period. After a careful validation process, rupture properties for a catalog of 96 earthquakes are obtained. The subsequent analysis of this catalog provides several insights about the seismic rupture process. We first report that up-dip ruptures are more abundant than down-dip ruptures for shallow subduction interface earthquakes, which can be understood as a consequence of the material contrast between the slab and the overriding crust. Rupture velocities, which are searched without any a-priori up to the maximal P wave velocity (6000–8000 m/s), are found between 1200 m/s and 4500 m/s. This observation indicates that no earthquakes propagate over long distances with rupture velocity approaching the P wave velocity. Among the 23 ruptures faster than 3100 m/s, we observe both documented supershear ruptures (e.g. the 2001 Kunlun earthquake), and undocumented ruptures that very likely include a supershear phase. We also find that the correlation of V_r with the source duration scaled to the seismic moment (T^s) is very weak. This directly implies that both T^s and V_r are anticorrelated with the stress drop $\Delta\sigma$. This result has implications for the assessment of the peak ground acceleration (PGA) variability. As shown by Causse and Song (2015), an anticorrelation between $\Delta\sigma$ and V_r significantly reduces the predicted PGA variability, and brings it closer to the observed variability.

1. Introduction

The moment rate functions, or source time functions (STFs), of an earthquake provide information on the spatio-temporal history of the rupture, integrated over the fault surface. STFs extracted from stations at different locations theoretically differ one from the other because of the rupture spatial finiteness, and are therefore referred as apparent STFs (ASTFs). In a simple unilateral rupture configuration (Haskell, 1964), the shapes of the ASTFs are affected by a simple directivity effect, depending on the rupture velocity to wave speed ratio and on the rupture propagation direction relative to the station location. Quantifying the directivity effect thus provides a direct way to constrain the rupture velocity and rupture propagation of an earthquake (e.g. Caldeira et al., 2010; Lengliné and Got, 2011; Park and Ishii, 2015; Warren and Shearer, 2006). The SCARDEC method (Vallée et al., 2011) provides access to the teleseismic P and SH ASTFs, that are extracted

through a deconvolution procedure in which focal mechanism, depth, and seismic moment are simultaneously retrieved. The method has then been validated by complementary approaches (Lentas et al., 2013) and finally routinely applied to all $M_w \geq 5.8$ earthquakes since 1992 (Vallée and Douet, 2016). It thus offers a database of thousands of events, available for tracking seismic source properties.

This database has so far been analyzed using averaged P ASTFs (available at http://scardec.projects.sismo.ipgp.fr), with the assumption that this average is a good proxy for the absolute STF. In this case, we have information on the macroscopic source parameters such as stress drop $\Delta\sigma$ or radiated energy Er, and we can explore their dependencies on seismic moment, depth or focal mechanism (Chounet and Vallée, 2014; Courboulex et al., 2016; Vallée, 2013). Such explorations have also been done at the global scale by a number of studies (e.g. Allmann and Shearer, 2009; Bilek et al., 2004; Convers and Newman, 2011; Dziewonski et al., 1981; Houston, 2001; Pérez-Campos

---

and Beroza, 2001), using first order features of moment tensors, other STFs catalogs, or source spectra. On the other hand, rupture finiteness only produces a second order effect on the seismic signals, making its extraction more difficult. For this reason, most of the related studies only analyze one or a few events, and exhaustive studies on rupture propagation properties have been so far uncommon.

Relevant past studies include McGuire et al. (2002) who analyzed the second moment of earthquakes over a catalog of 25 $M_w \geq 7$ earthquakes, and found that unilateral ruptures were strongly predominant, and Warren and Shearer (2006) who measured rupture directivity from P waves spectra for 66 worldwide earthquakes with the objective to resolve the fault plane ambiguity. Back-projections techniques locating high frequency emissions are now used more routinely, and in a recent study of Wang et al. (2016), they measured rupture speed for 23 large earthquakes, finding that strike–slip ruptures are faster than dip–slip ruptures. At the local scale, rupture directivity has been for example investigated at Parkfield on small earthquakes, through measurement of apparent source durations (Lengliné and Got, 2011), or earthquakes spectral azimuthal variations (Kane et al., 2013), in order to relate rupture directions with the fault interface materials.

The SCARDEC database provides the opportunity to significantly increase the number of moderate to large magnitude earthquakes for which rupture propagation characteristics can be extracted. We explore in this study how the P and S waves ASTFs properties can be systematically used, in order to measure average values of rupture propagation direction and rupture velocity. Applying the same methodology for all the analyzed earthquakes makes relative comparisons easier, compared to compilations of different studies using different data types and approaches. We focus here on shallow earthquakes (depth shallower than 120 km), and automatically detect earthquakes of the database which reliably have a dominant unilateral character. This leads us to a catalog of 96 earthquakes for which rupture propagation direction and rupture velocity can be investigated.

This catalog will be first used to characterize at the global scale how seismic rupture preferentially propagates. We will in particular discuss the relative abundance of fast earthquakes, possibly reaching supershear velocities (Bouchon et al., 2001; Dunham and Archuleta, 2004; Vallée and Dunham, 2012; Wang et al., 2016), as well as any predominance of rupture propagation directions between the up-dip or down-dip directions. The joint determination of rupture velocity, source duration and seismic moment also offers a more precise way to determine the static stress drop, compared to most techniques which neglect the effect of the rupture velocity. We will show that slow rupture velocities, as well as short rupture durations, tend to reveal high stress drop earthquakes. In other words, we observe an anticorrelation between rupture velocity and stress drop. This will be discussed in light of a recent study by Causse and Song (2015), who proposed this negative correlation to explain the observed variability of peak ground acceleration (PGA).

2. Systematic inversion of average rupture velocity and rupture direction using SCARDEC teleseismic apparent source time functions

2.1. Apparent STFs in a unilateral rupture model

During the earthquake, the rupture front propagates away from the hypocenter and spreads over the fault plane, emitting seismic waves in all directions. According to the directivity effect, emitted waves in the direction of rupture are shorter than expected for a point source, while those emitted away from the rupture direction are elongated. Consequently, if the rupture front has a dominant direction of propagation, a simple directivity pattern is observed on the distant records and on the ASTFs. Such a clear example of directivity can be observed for the Tokachi-oki Mw 8.1 subduction earthquake (2003/09/25, Japan, Fig. 1): the Tokachi-oki earthquake's ASTFs, shown in Fig. 1,

have shorter and more impulsive shapes for azimuths of about 325°, and more elongated ASTFs for azimuths of about 145°, evidencing a dominant down-dip rupture propagation along the subduction interface. Quantitatively, under an assumption of unilateral rupture with constant rupture propagation direction and rupture velocity, the ASTF duration (referred as the apparent duration τ) of an earthquake with fault dip δ, recorded at a station with azimuth θ (relative to the fault strike) and take-off angle i (see Fig. 2), follows the equation

$$\tau = T\left(1 + \frac{V_r}{C}\left(\sin(i)[\cos(\theta)\cos(\xi) + \sin(\theta)\sin(\xi)\cos(\delta)] + \cos(i)\sin(\xi)\sin(\delta)\right)\right), \quad (1)$$

where T and V_r are the source duration and rupture velocity respectively. ξ is the rupture direction angle defined on the fault plane, using the same convention as for the rake angle (see the sketch in Fig. 2). C is the phase velocity at the source of the considered body wave, and can be thus equal to the P wave velocity C_P or the S wave velocity C_S. Eq. (1) further considers that seismic slip is instantaneous (i.e. no rise time). Adding a rise time term in the equation is straightforward, but tests with real data showed that its value cannot be reliably retrieved. We here adopt a model of asymmetric triangular STF, where the apparent peak amplitude Fm is reached at a time $t_{Fm} = x_{Fm}T$, x_{Fm} being the asymmetry parameter varying between 0 and 1. In this triangular model, Fm follows the simple relation

$$Fm = \frac{2M_0}{\tau}, \quad (2)$$

where M_0 is the seismic moment. The ASTFs shape can thus be fully determined for each wave type and observation configuration, depending on four physical parameters T, V_r, x_{Fm}, and ξ. With a good geographical coverage, the observed ASTFs have a strong potential to reliably constrain the latter parameters. The practical implementation is given in the next section, but we discuss here our expected ability to systematically determine V_r with this formalism. First, the earthquake has to be dominantly unilateral. According to McGuire et al. (2002) observations, this latter property is the most common case, which can be understood in simple models where the hypocenter occurs in a random location inside a seismogenic patch. When the earthquake is not fully unilateral, we expect a tendency of underestimating V_r, while the dominant rupture direction ξ should not be significantly affected. This underestimation is reinforced by the instantaneous slip hypothesis, meaning that the full source duration is interpreted in terms of rupture propagation. These two reasons imply that the retrieved rupture velocity V_r has to be understood as a *lower bound* of the *average* rupture velocity. As a consequence, finding V_r close to C_S strongly indicates that at least part of the rupture occurred in the supershear regime. On the other hand, low rupture velocities can be difficult to interpret, because they can result from an earthquake with a bilateral or bidimensional rupture process, or from earthquakes with anomalously long rise time.

2.2. SCARDEC ASTFs analysis

2.2.1. Data selection

The resolution of the directivity pattern requires stations well distributed in azimuth, in particular because the coverage in take-off angles is intrinsically low with teleseismic data (i is in the range [20°–35°]). Due to the geographical gaps related to oceans, this condition is not always fulfilled, especially for small earthquakes ($Mw \simeq 6$). For large earthquakes, similar reasons result in unbalanced distributions of stations. To minimize this effect, we keep at most 3 stations in a 10° azimuth bin, and ensure that those stations are separated by at least 5° of epicentral distance.

ASTFs extracted close to the nodal planes of the teleseismic waves, or ASTFs producing large misfits between re-convolved signals and data are excluded. An earthquake is not analyzed when the station coverage
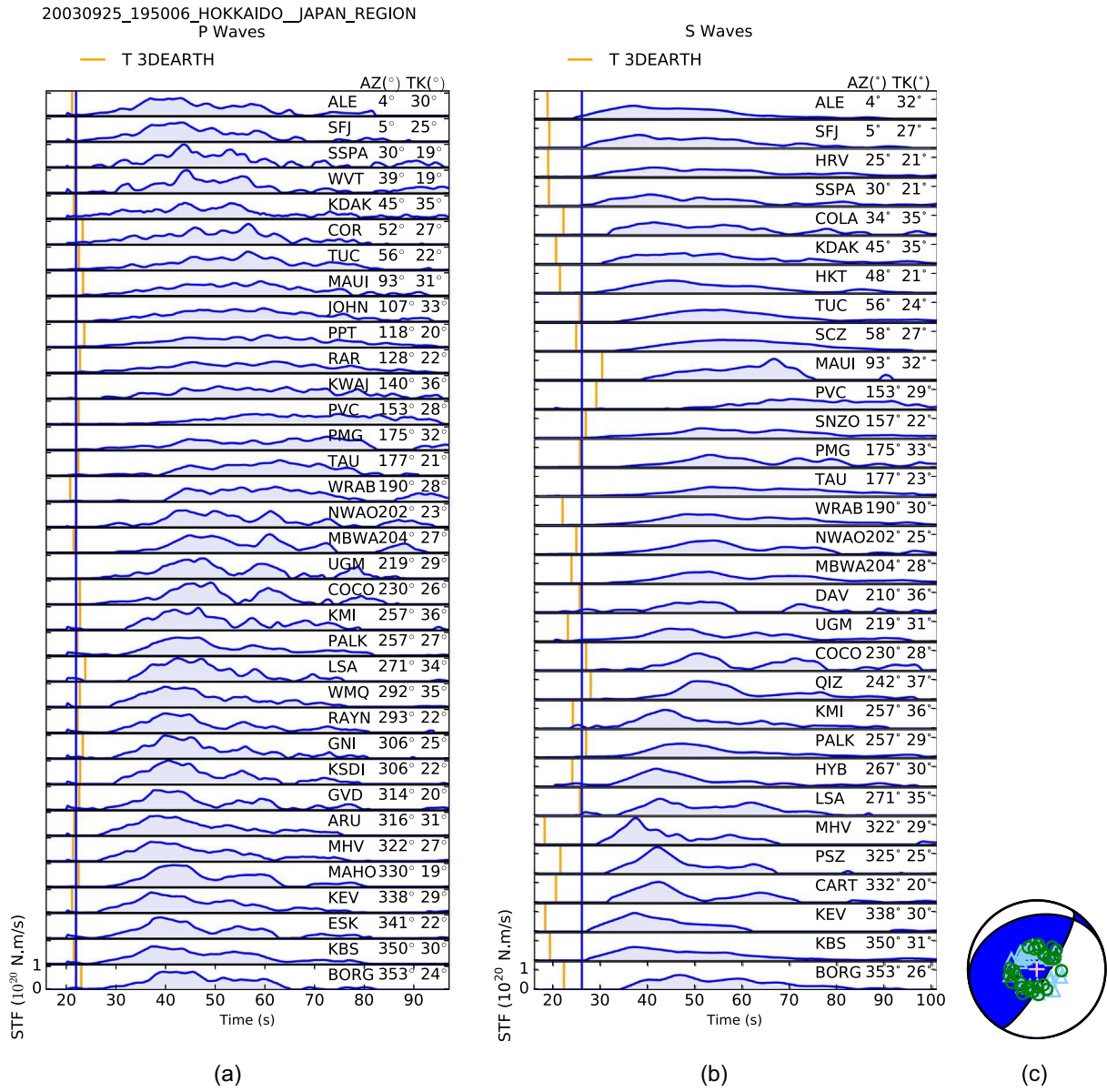
Fig. 1. P (a) and S (b) Apparent Source Time Functions for the 25/09/2003 Mw 8.1 Tokachi-oki earthquake, sorted by azimuth. ASTFs origin times in IASP91 (Kennett and Engdahl, 1991) and in a 3D Earth model (Simmons et al. (2012) for P waves, and Takeuchi (2012), for SH waves are marked by the blue and orange vertical ticks, respectively. (c) SCARDEC focal mechanism of the earthquake. The blue triangles and green circles represent the take-off angles for the P and S ASTFs, respectively. (For interpretation of the references to color in this figure legend, the reader is referred to the web version of this article.)
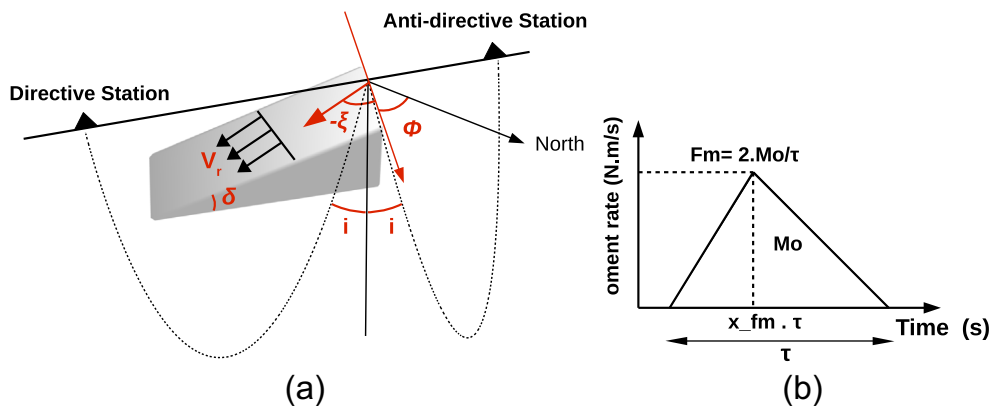
Fig. 2. (a) Sketch illustrating the rupture propagation model and the model parameters. The rupture direction, measured on the fault plane of dip δ, makes an angle ξ relative to the fault strike ϕ. ξ is negative when rupture is down-dip, and positive when rupture is up-dip. An illustration of directive and antidirective stations with their take-off angles (i) is shown. (b) Model parametrization of the triangular STF, with total apparent duration τ, seismic moment M_0, asymmetry x_{fm} and peak Fm.
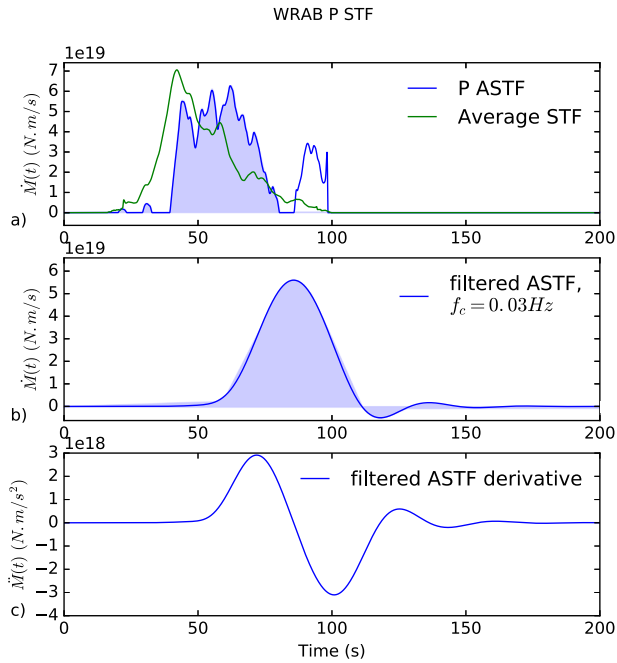
Fig. 3. (a) P ASTF at the station WRAB for the Tokachi-oki earthquake, and the superimposed average STF over correlated P ASTFs. Shaded area corresponds to the significant part of the function, consistent with the average STF. Late amplitudes (open area) are removed from the function. (b) Low-pass filtered function using the duration-dependent cut-off frequency, here equal to $f_c = 0.03$ Hz. (c) First derivative of the filtered ASTF, which is inverted for directivity parameters.

is too poor, when a large azimuthal gap is present for both P and S phases, or when too few stations are available (less than 16).

2.2.2. ASTFs complexity

Analysis of the ASTFs has the great advantage to give a direct access to the source term complexity. In the SCARDEC deconvolutive approach, this complexity can however be exaggerated because all un-modeled signals are mapped into the source term. For example, complexities in the Green function (not explained by a radial Earth model) or changes in the faulting mechanism are included in the ASTFs, which results in inconsistent amplitudes between the ASTFs (Vallée et al., 2011). Comparison between an ASTF and the averaged STF (obtained after stacking the re-correlated ASTFs) allows us to identify and remove late and inconsistent signals (Fig. 3).

The real source complexity also gives birth to ASTFs that cannot be directly compared to the triangular model defined by Eqs. (1) and (2). To overcome this, ASTFs are low-pass filtered, using an optimized cut-off frequency depending on the duration and level of complexity of the function (Fig. 3). This filter is accordingly applied to the triangular synthetic ASTFs.

2.2.3. Travel times errors corrections

Because of the use of a radial Earth structure model in the SCARDEC method (IASP91 Earth model, Kennett and Engdahl, 1991), travel time errors result in an imprecise beginning of the ASTFs. Errors of ± 2 s and ± 6 s are expected for the P and S waves ASTFs, respectively. Another source of timing error comes from the well-known trade-off between depth and origin time. P waves ASTFs should not be significantly affected (precisely because the location procedure with teleseismic data strongly relies on P wave arrivals), but S waves ASTFs can be globally shifted by a few seconds.

For earthquakes with moderate durations (between 15 and 30 s), the directivity effect modifies the apparent durations τ by a few seconds, which is on the order of the travel time errors. The actual beginning of the ASTFs could be searched, but a real slow start or a time

delay cannot be easily distinguished. We thus choose to correct travel times errors with 3D P and SH mantle tomography models, from Simmons et al. (2012) (P waves) and Takeuchi (2012) (SH waves). We compute predicted travel times using the LLNL-Earth3D 3D ray tracing code (https://www-gs.llnl.gov/about/nuclear-threat-reduction/nuclear-explosion-monitoring/global-3d-seismic-tomography). Results show a clear improvement in the prediction of the beginning of the P waves ASTFs (see Tokachi-oki example in Fig. 1). The beginning of S waves ASTFs is also globally better picked, even if some exceptions exist.

Real slow starts and origin time-location errors are taken into account with two time parameters Δt_P and Δt_S, that globally shift all the P and S ASTFs, respectively. After this correction, observed delays between actual and predicted beginnings for S ASTFs can still be of few seconds. An additional station-dependent shift of ± 3 s is therefore allowed in the optimization process for S ASTFs.

2.3. Inversion of sub-horizontal rupture propagations

2.3.1. Directivity from teleseismic data: limitation to sub-horizontal ruptures

Direct and surface-reflected body waves are merged in the teleseismic signal for shallow earthquakes. SCARDEC ASTFs therefore result from the deconvolution of the direct P and S phases together with the surface-reflected phases pP, sP (for P), and sS (for S). Depending on the rupture propagation direction, discrepancies can appear in the apparent durations and amplitudes between the direct and reflected phases: when rupture propagates steeply along dip, information on directivity carried by reflected phases (going up) and direct phases (going down) is inconsistent, and deconvolution of the associated signals results in invalid ASTFs in terms of directivity. In Eq. (1), this inconsistency between direct and reflected phases is associated with the term depending on $\frac{\cos(i)}{C}$, since this latter expression differs for the different phases considered in the deconvolution. This limitation does not affect the terms involving $\frac{\sin(i)}{C}$, because the ray parameter is essentially the same for P, pP and sP waves on the one hand, and S and sS on the other hand.

ASTFs can therefore be analyzed in terms of directivity only if the $\cos(i)$ term is dominated by the $\sin(i)$ terms in Eq. (1). This is the case when δ or ξ are small, or in other words when rupture is propagating sub-horizontally. This limitation is not expected to strongly affect the two main classes of earthquakes that will be explored. As the matter of fact, for subduction interplate earthquakes (occurring on the shallow-dipping subduction interface), the rupture direction ξ can be searched for all angles, and for large strike–slip earthquakes, the along strike horizontal propagation is dominant.

Depending on the radiation coefficients of direct and reflected phases, two versions of Eq. (1) are used. When both reflected and direct waves have significant amplitudes, we approximate τ by considering only the $\sin(i)$ term in Eq. (1):

$$\tau = T\left(1 + \frac{V_r}{C}\sin(i)[\cos(\theta)\cos(\xi) + \sin(\theta)\sin(\xi)\cos(\delta)]\right). \tag{3}$$

When the direct (respectively reflected) phases are close to be nodal, the ASTF essentially results from the deconvolution of the reflected (respectively direct) phases. In this case, Eq. (1) can be fully used with the take-off angle of the dominant phase, and provides a more accurate description of the directivity.

In Eq. (3), τ depends on $V_r\frac{\sin(i)}{C}$. As $\frac{\sin(i)}{C}$ is constant in a spherical Earth at a given depth, τ actually depends on V_r and not on $\frac{V_r}{C}$. As a consequence, the latter ratio (necessary to directly identify supershear earthquakes) requires the independent knowledge of C in the source volume. Given the limited knowledge of detailed crustal structure, absolute values of V_r are being considered in the following instead of $\frac{V_r}{C}$.

2.3.2. Inversion procedure

For each earthquake and each possible nodal plane, we search for 6 parameters: V_r, T, ξ, x_{fm} and the two P and S time delays Δt_P and Δt_S. All values of ξ are considered, but if the best solution indicates a rupture direction steeper than 30° (see Section 2.3.1), the earthquake is not included in the catalog.

The global misfit function m is the average of the normalized misfit functions between the derivatives of the ASTFs data and synthetics at each station (computed with a $L2$ norm):

$$m = \frac{1}{n_s} \sum_{i=1}^{n_s} \left(\frac{\int_0^{T_i} (\dot{D}_i(t) - \dot{S}_i(t))^2 dt}{\min \left(\int_0^{T_i} \dot{D}_i^2(t) dt, \int_0^{T_i} \dot{S}_i^2(t) dt \right)} \right), \qquad (4)$$

with n_s, D_i, S_i and T_i referring to the number of stations, ASTF data, ASTF synthetics and ASTF duration, respectively.

Optimization is performed using the Neighborhood Algorithm of Sambridge (1999). As our objective is to systematically detect earthquakes with reliable rupture propagation properties, we then apply the following selection criteria. Our selection first discards earthquakes with a global misfit $m \geq 0.6$, and then impose that directive and antidirective stations (controlling the directivity pattern) are specifically well fitted. To do so, we compute a weighted misfit where the 30% most directive and the 20% most antidirective stations have a weight of 3 and 2, respectively. Earthquakes with a weighted misfit $m_{weight} \geq 0.6$ are discarded. In order to further assess the reliability of the solution, we follow the idea of Warren and Shearer (2006), where the misfit of the best propagating model is compared to the misfit obtained with a point source. Here, we compute the ratio between the weighted misfit and the weighted point source misfit, r_{weight}. If this ratio is below 0.8, the solution is kept. Above this ratio, the best solution is too close to a point source to be considered reliable.

The last selection criteria are based on duration considerations. If the source duration is too short, or if the peak of moment rate release is too early, the expected variations between ASTFs are small and difficult to separate from timing uncertainties. Combining these two features, earthquakes with moment rate peaking at times shorter than 6 seconds are removed from catalog. This criterion also removes solutions with asymmetry x_{Fm} close to 0, which do not represent realistic STFs. Similarly, solutions with x_{Fm} above 0.95 are not kept, because they often try to accommodate complex shapes of STFs, and result in unrealistic solutions. The combined use of all these criteria finally provides a catalog of 96 earthquakes. The 2009/09/25 Tokachi-oki earthquake (Japan, $M_w = 8.1$, Fig. 4) is an example of these earthquakes with reliable rupture propagation properties. We obtain for this event a fast rupture velocity of $V_r = 3420$ m/s and a down-dip rupture direction along the slab, consistent with detailed source studies (e.g. Yagi, 2004).

Our Neighborhood Algorithm parametrization consists of 100 iterations with 30 new samples at each iteration, sampled in the neighborhood of the 25 previous best samples, which allows us to explore the parameter space around the best model. Weighted misfits are calculated for all the tested models. Models with weighted ratios within $r_{weight} + 5\% r_{weight}$ are used to establish the parameters uncertainties. Maps of the parameters space can be found in Fig. 5 for the Tokachi-oki earthquake, and provide a range of possible V_r between 2600 m/s and 3900 m/s, and a range of possible ξ between $-85°$ and $-40°$.

For all but 3 earthquakes, maximum and minimum possible values for V_r differ by less than 2000 m/s, and for half of the catalog, they differ by less than 1000 m/s. For rupture propagation angle, the maximum and minimum possible values differ by less than 90° for all but 2 earthquakes, and by less than 45° for the two thirds.

3. Rupture velocities and rupture propagation directions

Selected earthquakes are mainly thrust (56) and strike–slip (31) faulting events, with a minority of normal faulting earthquakes (9).

They are located on the map of Fig. 6. Histograms of earthquakes rupture parameters are shown in Fig. 7. Their moment magnitudes range between Mw 6 and Mw 8.8 (the largest earthquake is the 2010/02/27 Maule, Chile, earthquake), and the shortest earthquake durations are $\simeq 10$ s because of the criterion defined in the selection process. Rupture velocities span a range between 1200 m/s and 4500 m/s, with median values on the order of 2400 m/s. Most earthquakes of this catalog have roughly symmetric STFs, with an asymmetry ratio ranging between 0.3 and 0.6. The rupture parameters for the full catalog can be found in the Table S1 of the Supplementary material. In the following, we describe the content of the catalog in terms of rupture directions and rupture velocities, before discussing some implications for source parameters relations.

3.1. Rupture propagation directions

In Fig. 8, the rupture propagation direction angle ξ is shown as a function of the rake angle λ. Rupture propagation is considered along-strike when $\xi \in [-180°, -135°] \cup [-45°, 45°] \cup [135°, 180°]$, up-dip when $\xi \in [45°, 135°]$, and down-dip when $\xi \in [-135°, -45°]$. We observe a strong predominance of along-strike ruptures relative to along-dip ruptures (79 over 96 earthquakes). This is expected as it directly results from the selection bias of horizontal ruptures in our methodology. Isolating earthquakes with fault dip shallower than 30°, we can avoid this bias and estimate the proportion of along-strike to along-dip ruptures: for the 38 earthquakes with shallow dipping fault (mostly subduction interplate earthquakes), some differences remain with 16 along-dip ruptures and 22 along-strike ruptures. Such a rupture direction preference is naturally explained by the limited width of the seismogenic zone; however, the small differences also indicate that, even for this catalog including large earthquakes, the seismogenic zone is wide enough to allow a large diversity in rupture directions.

Among the along-dip ruptures, up-dip ruptures are more abundant than down-dip ruptures for thrust earthquakes. If we consider only the group of 13 along-dip subduction earthquakes, up-dip ruptures (9) are more than twice more abundant than down-dip ruptures (4) (Fig. 8). Interpretations of these observations should be made with care given the small number of events, but it has been proposed based on numerical studies (Andrews and Ben-Zion, 1997; Ben-Zion and Andrews, 1998) that when a fault surface is bimaterial, rupture toward the direction of slip of the most compliant rock is enhanced. From observations, preferential direction of rupture propagation related to material contrast has been for example found in the San Andreas Fault for microearthquakes (Kane et al., 2013; Lengliné and Got, 2011; Wang and Rubin, 2011). In subduction zones, the overriding crust is more compliant than the oceanic crust, which should encourage up-dip propagation for shallow interface ruptures. When the slab is in contact with the mantle wedge, the contrast is reversed and down-dip rupture should be favoured. Our observations agree with this depth partitioning, as none of the down-dip rupturing earthquakes occur at depths shallower than 24 km.

3.2. Rupture velocities

The average rupture velocities are represented according to their rupture modes in Fig. 9. The rupture mode R is defined based on the angle between rake and rupture directions, with the relation $R = |\xi - \lambda|$ $[\pi]$. R equal to 0° corresponds to in-plane rupture (mode II) and R equal to 90° corresponds to anti-plane rupture (mode III). As mentioned in Section 2.3.1, our methodology is sensitive to the absolute value of V_r, and V_r is therefore considered here rather than $\frac{V_r}{C_S}$. We first build a simple classification, separating the earthquakes with classical rupture velocities from earthquakes with fast rupture velocities. The limit between the two classes is set here to 3100 m/s, which is approximately equal to the Rayleigh wave velocity C_R ($\simeq 0.9 C_S$) in a standard crust
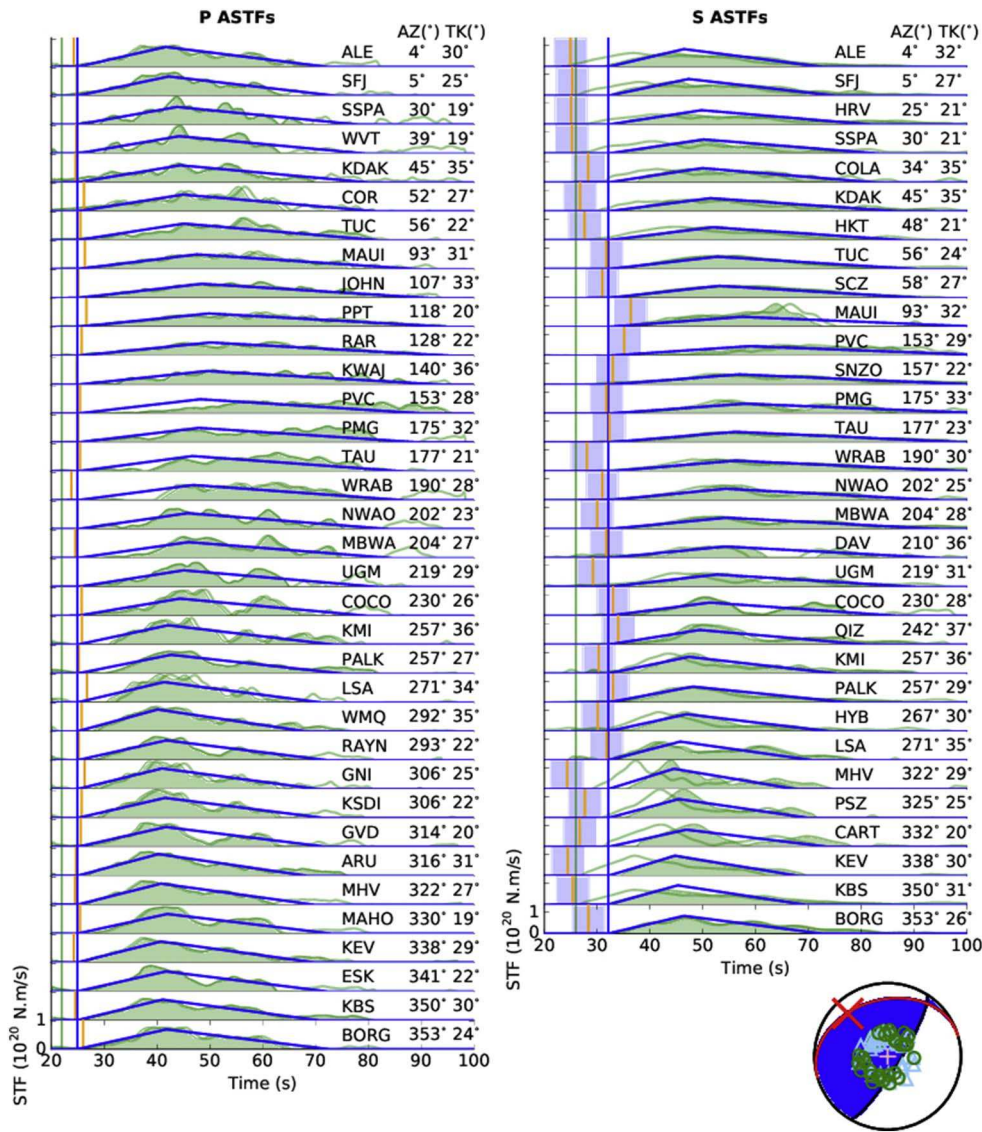
Fig. 4. Tokachi-oki earthquake raw ASTFs (light green line), processed ASTFs (green curve and shaded area), and triangular synthetic ASTFs of the best solution (blue line). ASTFs amplitudes and durations are well reproduced for a rupture (V_r = 3420 m/s) propagating toward the down-dip edge of the fault. Vertical green, blue, and orange ticks show the 1D origin time, the 3D origin time (see Fig. 1), and the effective start of ASTFs after inversion, respectively. Blue shaded stripes represent the range of time shift allowed in the inversion for each S ASTF. Earthquake focal mechanism is shown at the bottom of the figure, with the fault plane and the direction of propagation indicated in red. The blue triangles and green circles show the take-off angles of the stations for P and S ASTFs, respectively. (For interpretation of the references to color in this figure legend, the reader is referred to the web version of this article.)
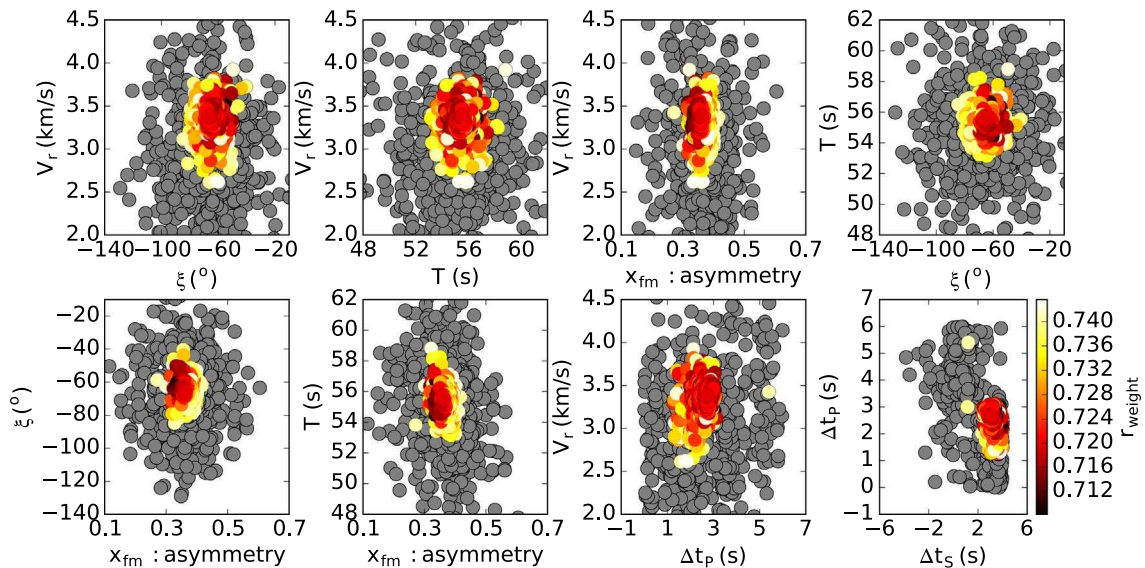
Fig. 5. Parameters of the model samples tested in the inversion for the shallow fault plane of the Tokachi-oki earthquake. Colored dots correspond to the accepted models, that differ from the ratio between the best model weighted misfit and the point source misfit by less than 5%. The ratio values are indicated by the colors. (For interpretation of the references to color in this figure legend, the reader is referred to the web version of this article.)

ARTICLE IN PRESS

A. Chounet et al.   Tectonophysics xxx (xxxx) xxx–xxx
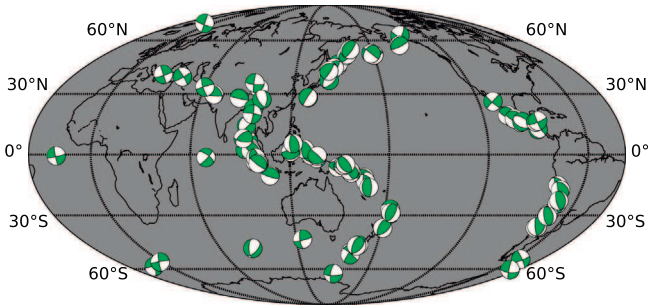
Fig. 6. Map of the 96 earthquakes of the catalog with their focal mechanisms.

Fig. 8. Direction of rupture propagation versus rake angle for the earthquakes of the catalog. Rupture propagation is determined by the angle ξ, measured relative to the fault strike (see Fig. 2). A positive angle indicates up-dip propagation, while negative angle indicates down-dip propagation. Orange stripes enlighten areas where earthquakes have a dominant up-dip or down-dip rupture direction. The color scale refers to the earthquakes depth. Subduction interface earthquakes which propagate along-dip are represented by triangles, and all the other earthquakes by circles. Bars correspond to uncertainties as defined in the text. (For interpretation of the references to color in this figure legend, the reader is referred to the web version of this article.)

model. Most earthquakes of our catalog (76 %) have classical rupture velocities ranging from 1200 m/s to C_R. As mentioned in Section 2.1, rupture velocities close to the former value have not to be directly interpreted as intrinsically slow, as the amount of bilaterality causes a rupture velocity underestimation. Table S1 shows for example that both the 2006/07/17 Java earthquake and the 2010/02/27 Maule earthquake are found with rupture velocities lower than 2000 m/s, but only the former earthquake is a real slow earthquake (Ammon et al., 2006). The rupture parameters of the 23 fast earthquakes (with V_r ranging from 3100 m/s to 4500 m/s) are displayed in Table 1.

According to crack theory (Andrews, 1976), in-plane rupture propagation can exceed the shear waves speed, with a forbidden zone between C_R and C_S. On the other hand, anti-plane rupture cannot theoretically propagate faster than C_S. We thus expect to find fast ruptures occurring in mode II. 7 of the 23 fast ruptures are observed in mode III (see Fig. 9 and Table 1) but they are all located below 30 km depth (and 5 of them between 40 km and 80 km) (Fig. 9). In this range of depth, C_S is likely to be close from classical upper mantle velocities ($\simeq$4500 m/s), and thus $\frac{V_r}{C_S}$ remains below unity.

Most of the fast mode II ruptures (11 of 16) are found for strike–slip faulting earthquakes. Interestingly, for the other fast events, two earthquakes occur in similar locations with close characteristics: the 2003/09/25 Mw 8.1 Tokachi-oki earthquake and the 1994/12/28 Mw 7.7 Sanriku-oki earthquake (located in the north-east part of Japan trench) both have rupture velocities above 3400 m/s and down-dip rupture propagation.

Some of the fast strike–slip earthquakes correspond to well-known events. The supershear Kunlun earthquake (2001/11/14, Bouchon and Vallée, 2003, Vallée and Dunham, 2012) is part of this group, with an average V_r of 3407 m/s, consistent with the overall rupture speed, which was slow at its beginning. We find a similar behaviour for the Denali earthquake (2002/11/03, V_r = 3458 m/s), consistent with a supershear phase (Dunham and Archuleta, 2004), preceded and followed by a subshear regime. The 2003/07/15 Mw 7.6 Carlsberg earthquake is found to rupture at a very high rupture velocity of V_r = 4250 m/s, even faster that the velocity determined by Antolik et al. (2006) ($V_r \simeq$ 3500 m/s). Wang et al. (2016) also reported a fast rupture velocity (V_r = 3470–3950 m/s) for this event. Some other earthquakes

Fig. 9. Rupture velocity versus rupture mode for the earthquakes of the catalog. The color scale refers to the earthquakes depth. Strike–slip, reverse, and normal faulting earthquakes are shown by circles, triangles, and squares, respectively. Bars correspond to uncertainties as defined in the text. (For interpretation of the references to color in this figure legend, the reader is referred to the web version of this article.)

found as supershear in the literature are not present in our catalog. In particular, the 1999/08/17 Izmit earthquake (Bouchon et al., 2001) had a bilateral rupture and the 2013/01/05 Mw 7.5 Craig earthquake (Yue et al., 2013) is not included in the catalog because of its too complex ASTFs.

Our catalog also displays strike–slip earthquakes that were not clearly identified as fast or supershear earthquakes. The clearest

Fig. 7. Histograms of the catalog source parameters: (a) Moment magnitude, (b) source duration, (c) rupture velocity, (d) rupture direction over the fault plane, and (e) asymmetry of the source time function.

Table 1
Rupture propagation parameters of the 23 fast rupture earthquakes of the catalog.

Event	z	Mw	Rake	V_r (min, max)	T	Rupture propagation	Rupture mode
	(km)		(°)	(m/s)	(s)	(azimuth, dip) (°)	(min, max) (°)
19941228 Off East Coast of Honshu Japan	27	7.7	64	3718 (3016, 4010)	54	(274, −15)	19 (12, 30)
19960723 South of Fiji Islands	8	6.5	−43	4130 (2517, 4496)	22	(111, 2)	40 (14, 43)
19970510 Northern and Central Iran	19	7.3	175	3162 (2867, 3606)	40	(164, −5)	1 (5, 10)
20011114 Qinghai China	21	7.9	−8	3406 (3097, 3671)	117	(96, −1)	7 (3, 11)
20021103 Central Alaska	25	7.9	−162	3458 (3254, 3769)	81	(119, −1)	19 (13, 25)
20030715 Carlsberg Ridge	22	7.6	−150	4254 (3659, 5064)	63	(43, 0)	30 (24, 36)
20030925 Hokkaido Japan Region	43	8.1	130	3420 (2613, 3922)	55	(317, −18)	15 (10, 35)
20071110 North of Macquarie Island	23	6.6	168	4076 (3596, 4351)	24	(37, 2)	11 (4, 12)
20090528 North of Honduras	24	7.4	−7	4105 (3286, 5371)	55	(241, −24)	32 (36, 45)
20100616 Irian Jaya Indonesia	13	7.0	−162	3187 (2617, 3862)	24	(336, −2)	20 (9, 33)
20120830 Jan Mayen Island Region	14	6.8	0	3183 (3014, 3724)	22	(111, −7)	8 (7, 15)
20130201 Santa Cruz Islands	21	6.4	64	3374 (3039, 3818)	14	(227, 19)	15 (12, 17)
20131024 East of South Sandwich Islands	29	6.7	9	3129 (2710, 3649)	27	(261, −14)	5 (8, 29)
20131125 Falkland Islands Region	16	7.0	12	3406 (2937, 4182)	26	(71, −7)	18 (7, 23)
20141014 Off Coast of Central America	54	7.2	−90	3683 (2945, 4268)	18	(206, −17)	14 (4, 36)
20150329 New Britain Region P.N.G.	43	7.5	90	3177 (2028, 3369)	30	(169, 29)	1 (6, 18)
19990119 New Ireland Region P.N.G.	76	7.1	92	3892 (3845, 4295)	23	(149, 8)	78 (82, 87)
19991117 New Britain Region P.N.G.	46	7.0	90	3389 (2588, 3969)	19	(129, −27)	56 (28, 69)
20001117 New Britain Region P.N.G.	51	7.5	87	4067 (2841, 4982)	38	(50, −18)	49 (34, 69)
20041122 Off W. Coast Of S. Island N.Z.	36	7.1	109	4494 (3795, 5093)	15	(52, −5)	63 (53, 78)
20050909 New Ireland Region P.N.G.	78	7.7	89	3350 (3140, 3802)	60	(151, −7)	77 (65, 90)
20100612 Nicobar Islands India Region	31	7.4	47	3425 (2691, 4456)	30	(53, 5)	54 (47, 66)
20111021 Kermadec Islands Region	47	7.4	80	3992 (3492, 5301)	18	(44, 20)	68 (43, 87)

example is likely the 2009/05/28 Mw 7.4 Honduras earthquake, for which we find a rupture duration of 55 s and a rupture velocity of 4105 m/s. Our findings are strongly supported by the associated rupture length of 226 km, consistent with the GPS and aftershock study of Graham et al. (2012). With a depth of 24 km, this earthquake is very likely to have at least a large part of its rupture in the supershear regime. The 1997/05/10 Mw 7.3 Zirkuh earthquake in Iran, with $V_r = 3162$ m/s for a 40 s duration, leads to a rupture length of 126 km, also consistent with surface ruptures observations (Sudhaus and Jónsson, 2011). We also find a group of earthquakes with moderate magnitudes ($6.6 \leq M_w \leq 7$) and fast ruptures (3100 m/s $\leq M_w \leq 4100$ m/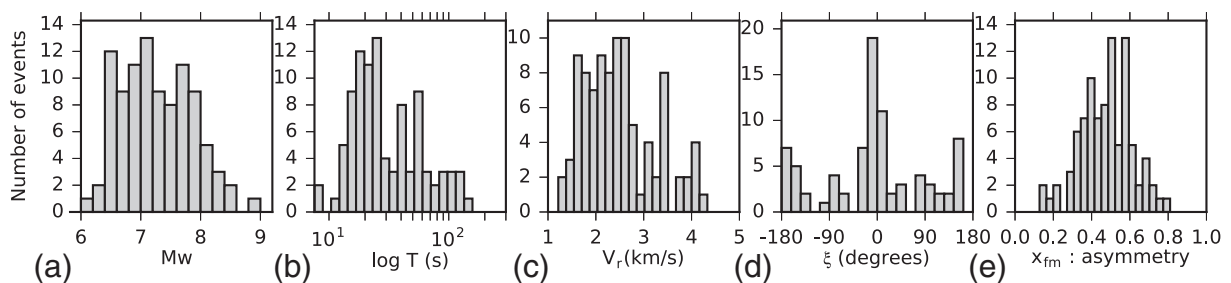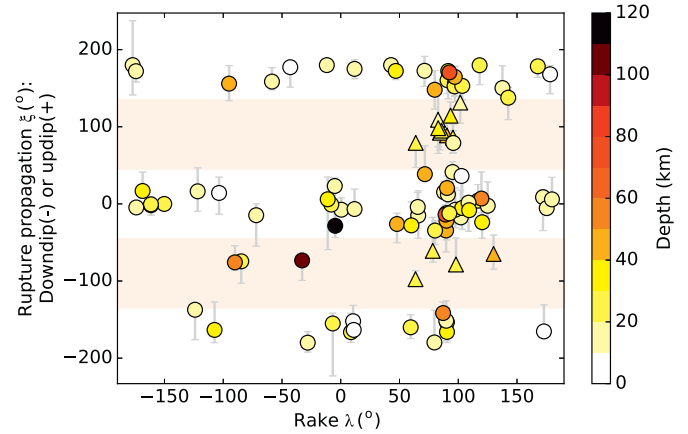s) along the oceanic transform faults. This is the case of the 2007/11/10 Macquarie, the 2012/08/30 Jan Mayen, the 2013/10/24 South Sandwich and the 2013/11/25 Falkland earthquakes. These events directly show that fast ruptures are not limited to very large earthquakes.

Given the uncertainties in V_r and C_S, and the fact that we only detect average properties, it is difficult to assert the presence of a supershear phase during the earthquake rupture propagation. On the other hand, we show that earthquakes very rarely have their whole rupture propagation in the supershear regime, and that they do not appear to propagate at the P wave velocity over long distances. Our catalog confirms that most of the earthquakes propagate in the subshear regime, and that faster earthquakes exist, but clearly remains a minority.

4. Anticorrelation between stress drop and rupture velocity

4.1. Stress drop estimation including rupture velocity determinations

In observational seismological studies, systematic estimates of earthquakes source parameters are of key interest. For example, the static stress drop $\Delta\sigma$ describes if the rupture is compact or spread out, with $\Delta\sigma \propto \mu\Delta\epsilon$ (μ is the rigidity and the strain drop $\Delta\epsilon$ is itself proportional to ratio of the average slip to the fault dimension). $\Delta\sigma$ can be estimated from the corner frequency (f_c) of the source spectra in a Brune's model (Brune, 1970) (e.g. Allmann and Shearer, 2009; Uchide et al., 2014), where f_c varies as $V_r \Delta\sigma^{1/3}$. Assuming that V_r is a constant proportional to C_S, $f_c \propto \Delta\sigma^{1/3}$ and the stress drop can be calculated. Another approach is to measure the moment-scaled duration T^s (or,

similarly the moment-scaled peak) from STFs (done for example with the SCARDEC database by Vallée (2013) and Courboulex et al. (2016)), which varies as $\frac{1}{V_r \Delta\sigma^{\frac{1}{3}}}$ for a bi-dimensional growing rupture. Similarly as for f_c, the conversion of T^s into stress drop implies that V_r is a constant proportional to C_S. However, if the latter assumption is not valid, characterizing variations of f_c or T^s in terms of stress drop variations can be misleading. If the ambiguity cannot be resolved, f_c or T^s variations should be related to both $\Delta\sigma$ and V_r variations (Chounet and Vallée, 2014). This ambiguity may also be problematic for characterizing the stress drop variability. For instance, Kaneko and Shearer (2015) showed that the stress drop variability revealed by f_c-based studies may be essentially attributed to variations of the rupture velocity.

In this study, the independent measurement of V_r, T and M_0 allows us to estimate the stress drop variations and to explore the possible interlinks between V_r, T^s, and $\Delta\sigma$. We first proceed assuming a bi-dimensional model, which will be discussed in a second step in light of our dataset. Derivation of the seismic moment expression in a bi-dimensional rupture model gives:

$$M_0 \propto \mu D L^2,$$
$$M_0 \propto \Delta\sigma L^3,$$
$$M_0 \propto \Delta\sigma (T V_r)^3, \tag{5}$$

$$\Delta\sigma \propto \frac{M_0}{(T V_r)^3}, \tag{6}$$

where D is the average slip, and L the rupture length, with $L = T V_r$. Introducing the moment-scaled duration, $T^s = T\left(\frac{M_0^{ref}}{M_0}\right)^{1/3}$ ($M_0^{ref} = 10^{19}$ N·m) in Eq. (6), it appears that T^s varies as $\frac{1}{V_r \Delta\sigma^{1/3}}$. In Eq. (6), $\Delta\sigma$ variations thus depend on two parameters independently obtained (T^s and V_r), that might be correlated or not. In case of independence between $\Delta\sigma$ and V_r, an anticorrelation between T^s and V_r should be observed. A representation of T^s as a function of V_r is shown in Fig. 10 (a). From our catalog, no correlation between these two parameters is found ($C = -0.04$, with $C = \frac{Cov(T_{\log}^s, V_{r\ \log})}{\sqrt{Var(T_{\log}^s).Var(V_{r\ \log})}}$, with Cov being the covariance, Var the variance, and $X_{\log}$ referring to the decimal logarithm of variable X). It is noteworthy to mention that no correlation is found between M_0 and V_r, between T and V_r, or between T^s and M_0 from our dataset. We then compute a parameter proportional
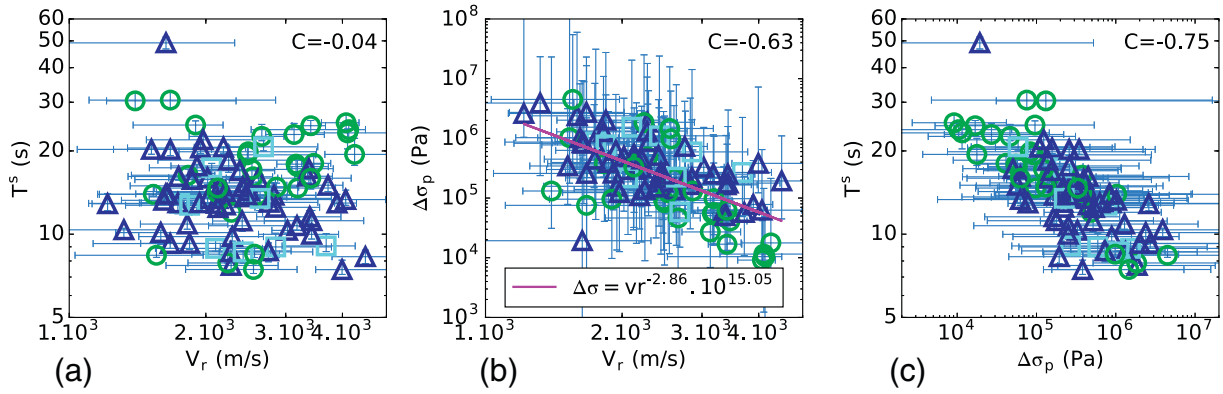
Fig. 10. (a) Scaled duration T^s (with a bi-dimensional scaling) versus rupture velocity for all the earthquakes of the catalog. (b) $\Delta\sigma_p$ versus V_r. (c) $\Delta\sigma_p$ versus T^s. For the three subfigures, the corresponding correlation coefficient is shown. A linear regression is proposed (magenta line and equation in the inset) between $\log(\Delta\sigma_p)$ and $\log(V_r)$. The three colors indicate the faulting type: blue triangles, light blue squares, and green circles represent thrust, normal, and strike–slip earthquakes, respectively. (For interpretation of the references to color in this figure legend, the reader is referred to the web version of this article.)

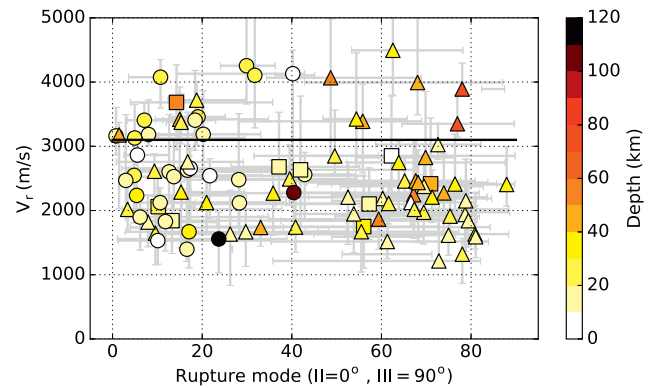to stress drop, referred as $\Delta\sigma_p$, using Eq. (6): $\Delta\sigma_p = \frac{M_0}{(TV_r)^3}$. $\Delta\sigma_p$ has the dimension of a stress drop (Pa), but its absolute value should not be directly compared to an actual stress drop value because no proportionality constant is set to estimate it. Rather than computing absolute stress drop estimates which can suffer from rupture model assumptions, we here prefer to focus on the variations of the stress drop with respect to the other source parameters. As expected from the absence of correlation between T^s and V_r, the stress drop $\Delta\sigma_p$ and the rupture velocity V_r are significantly anticorrelated ($C = -0.63$, Fig. 10 (b)). Consistently, we find that the normalized source duration T^s is strongly anticorrelated with the stress drop ($C = -0.75$, Fig. 10 (c)), which supports stress drop estimates using f_c or T^s. No significant correlation is found between $\Delta\sigma_p$ and M_0, and between $\Delta\sigma_p$ and T ($C = 0.3$ and $C = 0.02$, respectively, the larger C found for M_0 being related to the selection bias of small earthquakes with long durations, explained in Section 2.3.2).

Our dataset consists of ruptures whose directions of propagation are dominantly unilateral, so that their directivity can be explained by a Haskell-like model. In the original Haskell model, rupture starts from a line of width W, which produces a uni-dimensional scaling. However, this end-member scaling is not well-suited for most ruptures of our catalog. In real ruptures, unless L is significantly larger than W, the rupture growing from hypocenter spreads over the fault surface for the major part of the moment rate release, and hence, scales as a bi-dimensional rupture. Here, the uni-dimensional /bi-dimensional terms refer to the growth of the ruptured area, while the unilateral/bilateral terms refer to the asymmetry of hypocenter location relative to the ruptured area. Based on the subset of earthquakes with M_0 larger than $3 \cdot 10^{19}$ N·m (which avoids the selection bias of smaller magnitude

earthquakes with long durations), the linear regression between $\log(M_0)$ and $\log(T)$ provides a slope of 0.32, which means that most of the unilateral earthquakes of our catalog are bi-dimensional. This can be explained in our catalog by the abundance of thrust subduction earthquakes, which can rupture both along-dip or along-strike (see Section 3.1), implying that in most of these cases the rupture length to rupture width ratio, $\frac{L}{W}$, does not reach large values.

Ruptures with large $\frac{L}{W}$ ratio however exist (in particular the long strike–slip earthquakes), and in this case of uni-dimensional growth, stress drop should be computed using $\frac{D}{W}$, i.e. the ratio of average slip to the smallest fault dimension (e.g. Scholz, 1982). Thus, in a constant stress drop hypothesis, seismic moment should scale with rupture length L, instead of L^3 in the bi-dimensional case (e.g. Romanowicz, 1992; Scholz, 1982). However, analysis of sparse catalogs of long ruptures has led to different conclusions. Whether slip grows with W (Romanowicz, 1992; Romanowicz and Ruff, 2002), implying a constant stress drop with M_0, or with L (Scholz, 1982), implying an increasing stress drop with M_0, has been an ongoing controversy. More complex interpretations where slip grows with L, but at a decreasing rate, have also been proposed (Mai and Beroza, 2000; Shaw and Scholz, 2001). Such analyses based on our catalog are not possible because of the too small number of long ruptures. We thus prefer to exclude the long ruptures, and consider here a catalog consistent with the bi-dimensional assumption. For strike–slip and normal faulting earthquakes, ruptures with $L \geq 80$ km, and for thrust faulting earthquakes, ruptures with $L \geq 250$ km, are considered as uni-dimensional and hence, excluded. This removes 14 earthquakes over 96, with 13 strike–slip or normal faulting earthquakes, and 1 thrust faulting earthquake (the 2006/07/17 Mw 7.8 Java earthquake). Using the reduced catalog, the Fig. 11 (a) shows
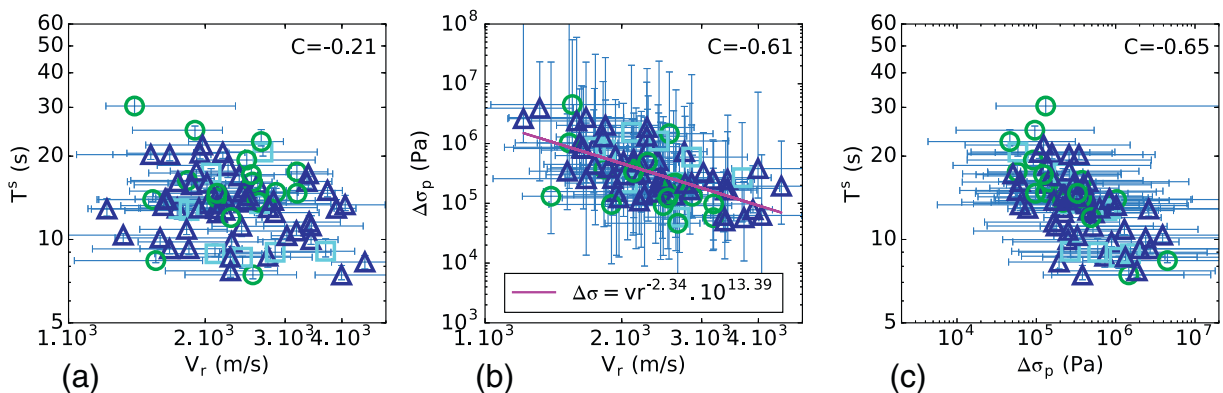
Fig. 11. (a), (b) and (c) Same as Fig. 10, but after removal of the earthquakes with a uni-dimensional rupture character.

almost no correlation between T^s and V_r ($C = -0.21$). The difference in correlation coefficient between Figs. 10 (a) and 11(a) can be attributed to the removal of both fast and long duration ruptures (i.e. long ruptures) of the catalog. The anticorrelation between $\Delta\sigma_p$ and V_r is still observed, with a coefficient ($C = -0.63$) similar to the value found for the whole catalog (Fig. 11 (b)), and stress drop is also anticorrelated with T^s ($C = -0.65$, Fig. 11 (c)). We see in Figs. 10 and 11 that the correlations trends do not depend on faulting type.

Our observations indicate that for a given seismic moment, a large average rupture velocity is not compensated by a short source duration, and therefore tends to favor low strain drops and low stress drops. A similar observation was found during the 2003 Big Bear sequence (Tan and Helmberger, 2010), using apparent STFs of earthquakes with $Mw \simeq 3 - 5$. A physical explanation of this anticorrelation can be found when considering the plastic off-fault damage during rupture propagation. As shown by numerical experiments of dynamic ruptures (Gabriel et al., 2013; Templeton and Rice, 2008), the off-fault plastic deformation reduces rupture speed because less energy is available for rupture propagation. These experiments also show that intensity and extension of the off-fault plasticity are increased when the surrounding rocks undergo a high stress level, making them closer to the elastic-plastic transition. Such conditions of high pre-stress finally offer the potential for a large stress drop when rupture occurs, meaning that large stress drops are expected to preferentially occur in contexts prone to off-fault damage. Although high stress drop would favor rupture propagation in a purely elastic case, the numerical simulations of Gabriel et al. (2013) suggest that the effect of off-fault plastic deformation on rupture velocity can become dominant, resulting in an anticorrelation between stress drop and rupture velocity. We finally report the work of Manighetti et al. (2007), who found from fault slip profiles that stress drop is reduced for ruptures on mature faults relative to immature ones. Combined with the recent work of Perrin et al. (2016) who observed that mature faults tend to favor fast rupture velocities, these studies also suggest that rupture velocity and stress drop are anticorrelated.

4.2. Implication for ground motion variability

Seismic hazard studies require the prediction of ground motions caused by potential future earthquakes, including an estimation of the median and the variability. At high frequency, the ground motion is classically represented by the Peak Ground Acceleration (PGA), which is commonly related to the corner frequency using the random vibration theory. Assuming a classical Brune source model (Brune, 1970) with constant rupture velocity, Cotton et al. (2013) obtained that: $PGA \propto f_c^{5/2} \propto \Delta\sigma^{5/6}$ and hence:

$$\sigma_{PGA} \propto \frac{5}{6}\sigma_{\Delta\sigma}, \tag{7}$$

where σ_{PGA} and $\sigma_{\Delta\sigma}$ are the variability of PGA and $\Delta\sigma$, respectively, assuming log-normal distributions. As such, the variability in stress drop directly affects all ground motion simulations. Using Eq. (7), Cotton et al. (2013) showed that if the stress drop variability is calibrated from f_c-based measurements, the obtained PGA variability is far above the observed between-event variability reported by Ground Motion Prediction Equations. Oth et al. (2017) reached the same conclusion by analyzing a dataset of $\simeq 1900$ Japanese events. Recently, Causse and Song (2015) used a similar approach as Cotton et al. (2013) but removed the assumption of a constant rupture velocity. They obtained that the PGA variability is then expressed as:

$$\sigma_{PGA} = \sqrt{5.76\sigma_{V_r}^2 + 0.64\sigma_{\Delta\sigma}^2 + 3.84\sigma_{V_r}\cdot\sigma_{\Delta\sigma}\cdot CORR}, \tag{8}$$

where σ_{V_r} is the rupture velocity variability and CORR is the coefficient of correlation between $\log(\Delta\sigma)$ and $\log(V_r)$. Eq. (8) shows that the anticorrelation revealed by our analysis of source time functions ($CORR = -0.61$) is an effective way to reduce the PGA variability.

Causse and Song (2015) suggest that $CORR < -0.5$ is necessary to match the observed PGA between-event variability. Considering anticorrelation between stress drop and rupture may then be important for designing suitable rupture scenarios for seismic hazard studies. It is noteworthy that Eq. (8) only depends on the average stress drop and the average rupture velocity and is based on the random vibration theory. The PGA is also affected by local source processes at characteristic frequencies larger than f_c, which may modify Eq. (8) (Archuleta and Ji, 2016).

5. Conclusion

Using the directivity of the SCARDEC apparent source time functions, we were able to quantitatively constrain the average rupture velocity and rupture propagation for earthquakes ($M_w \geq 6$) with dominant unilateral ruptures. This automatic method is successfully applied to 96 earthquakes that exhibit resolvable directivity. The earthquakes rupture propagations show a predominance of up-dip relative to down-dip propagation in subduction context. This general tendency can be related to the material contrast across the subduction interface. Fast ruptures, that possibly include a supershear phase, are observed for a minority of earthquakes (23), with both strike–slip and dip–slip mechanisms. This subgroup includes some well-known supershear ruptures and also undocumented events (with Mw between 6.4 and 7.5). The combined measurement of seismic moment, rupture velocity and rupture duration provides an estimate of the stress drop. We show from our catalog that rupture velocity is anticorrelated with the stress drop. For example, slow rupture and large slip for tsunami-earthquakes support this observation. Such anticorrelation provides a clue to understand the discrepancy between observed and predicted peak ground acceleration (PGA) variability. As shown by Causse and Song (2015), anticorrelation between stress drop and rupture velocity reduces the predicted PGA variability, and brings it closer to the observed variability.

Supplementary data to this article can be found online at http://dx.doi.org/10.1016/j.tecto.2017.11.005.

References

Allmann, B.P., Shearer, P.M., 2009. Global variations of stress drop for moderate to large earthquakes. J. Geophys. Res. Solid Earth (1978-2012) 114 (B1).

Ammon, C.J., Kanamori, H., Lay, T., Velasco, A.A., 2006. The 17 July 2006 Java tsunami earthquake. Geophys. Res. Lett. 33 (24).

Andrews, D., 1976. Rupture velocity of plane strain shear cracks. J. Geophys. Res. 81 (32), 5679–5687.

Andrews, D.J., Ben-Zion, Y., 1997. Wrinkle-like slip pulse on a fault between different materials. J. Geophys. Res. Solid Earth 102 (B1), 553–571.

Antolik, M., Abercrombie, R.E., Pan, J., Ekström, G., 2006. Rupture characteristics of the 2003 Mw 7.6 mid-Indian Ocean earthquake: implications for seismic properties of young oceanic lithosphere. J. Geophys. Res. Solid Earth 111 (B4).

Archuleta, R.J., Ji, C., 2016. Moment rate scaling for earthquakes $3.3 \leq m \leq 5.3$ with implications for stress drop. Geophys. Res. Lett. 43 (23).

Ben-Zion, Y., Andrews, D., 1998. Properties and implications of dynamic rupture along a material interface. Bull. Seismol. Soc. Am. 88 (4), 1085–1094.

Bilek, S., Lay, T., Ruff, L., 2004. Radiated seismic energy and earthquake source duration variations from teleseismic source time functions for shallow subduction zone thrust earthquakes. J. Geophys. Res. Solid Earth (1978-2012) 109 (B9).

Bouchon, M., Bouin, M.P., Karabulut, H., Toksöz, M.N., Dietrich, M., Rosakis, A.J., 2001.

How fast is rupture during an earthquake? New insights from the 1999 Turkey earthquakes. Geophys. Res. Lett. 28 (14), 2723–2726.

Bouchon, M., Vallée, M., 2003. Observation of long supershear rupture during the magnitude 8.1 Kunlunshan earthquake. Science 301 (5634), 824–826.

Brune, J.N., 1970. Tectonic stress and the spectra of seismic shear waves from earthquakes. J. Geophys. Res. 75 (26), 4997–5009.

Caldeira, B., Bezzeghoud, M., Borges, J.F., 2010. DIRDOP: a directivity approach to determining the seismic rupture velocity vector. J. Seismol. 14 (3), 565–600.

Causse, M., Song, S.G., 2015. Are stress drop and rupture velocity of earthquakes independent? Insight from observed ground motion variability. Geophys. Res. Lett. 42 (18), 7383–7389.

Chounet, A., Vallée, M., 2014. Systematic Characterization of Radiated Energy and Static Stress Drop of Global Subduction Earthquakes from Source Time Functions Analysis. AGU Fall Meeting Abstracts (Vol. 1, p. 01).

Convers, J., Newman, A., 2011. Global evaluation of large earthquake energy from 1997 through mid-2010. J. Geophys. Res. Solid Earth 116 (B8).

Cotton, F., Archuleta, R., Causse, M., 2013. What is sigma of the stress drop? Seismol. Res. Lett. 84 (1), 42–48.

Courboulex, F., Vallée, M., Causse, M., Chounet, A., 2016. Stress-drop variability of shallow earthquakes extracted from a global database of source time functions. Seismol. Res. Lett

Dunham, E.M., Archuleta, R.J., 2004. Evidence for a supershear transient during the 2002 Denali Fault earthquake. Bull. Seismol. Soc. Am. 94 (6B), S256–S268.

Dziewonski, A., Chou, T.A., Woodhouse, J., 1981. Determination of earthquake source parameters from waveform data for studies of global and regional seismicity. J. Geophys. Res. Solid Earth (1978-2012) 86 (B4), 2825–2852.

Gabriel, A.A., Ampuero, J.P., Dalguer, L., Mai, P.M., 2013. Source properties of dynamic rupture pulses with off-fault plasticity. J. Geophys. Res. Solid Earth 118 (8), 4117–4126.

Graham, S.E., DeMets, C., DeShon, H.R., Rogers, R., Maradiaga, M.R., Strauch, W., Wiese, K., Hernandez, D., 2012. GPS and seismic constraints on the $m = 7.3$ 2009 Swan Islands earthquake: implications for stress changes along the Motagua Fault and other nearby faults. Geophys. J. Int. 190, 1625–1639.

Haskell, N., 1964. Total energy and energy spectral density of elastic wave radiation from propagating faults. Bull. Seismol. Soc. Am. 54 (6A), 1811–1841.

Houston, H., 2001. Influence of depth, focal mechanism, and tectonic setting on the shape and duration of earthquake source time functions. J. Geophys. Res. Solid Earth (1978-2012) 106 (B6), 11137–11150.

Kane, D.L., Shearer, P.M., Goertz-Allmann, B.P., Vernon, F.L., 2013. Rupture directivity of small earthquakes at Parkfield. J. Geophys. Res. Solid Earth 118 (1), 212–221.

Kaneko, Y., Shearer, P., 2015. Variability of seismic source spectra, estimated stress drop, and radiated energy, derived from cohesive-zone models of symmetrical and asymmetrical circular and elliptical ruptures. J. Geophys. Res. Solid Earth 120 (2), 1053–1079.

Kennett, B., Engdahl, E., 1991. Traveltimes for global earthquake location and phase identification. Geophys. J. Int. 105 (2), 429–465.

Lengliné, O., Got, J.-L., 2011. Rupture directivity of microearthquake sequences near Parkfield, California. Geophys. Res. Lett. 38 (8).

Lentas, K., Ferreira, A., Vallée, M., 2013. Assessment of SCARDEC source parameters of global large (Mw 7.5) subduction earthquakes. Geophys. J. Int. 195 (3), 1989–2004.

Mai, P.M., Beroza, G.C., 2000. Source scaling properties from finite-fault-rupture models. Bull. Seismol. Soc. Am. 90 (3), 604–615.

Manighetti, I., Campillo, M., Bouley, S., Cotton, F., 2007. Earthquake scaling, fault segmentation, and structural maturity. Earth Planet. Sci. Lett. 253 (3), 429–438.

McGuire, J.J., Zhao, L., Jordan, T.H., 2002. Predominance of unilateral rupture for a global catalog of large earthquakes. Bull. Seismol. Soc. Am. 92 (8), 3309–3317.

Oth, A., Miyake, H., Bindi, D., 2017. On the relation of earthquake stress drop and ground motion variability. J. Geophys. Res. Solid Earth.

Park, S., Ishii, M., 2015. Inversion for rupture properties based upon 3-d directivity effect and application to deep earthquakes in the Sea of Okhotsk region. Geophys. J. Int. 203 (2), 1011–1025.

Pérez-Campos, X., Beroza, G.C., 2001. An apparent mechanism dependence of radiated seismic energy. J. Geophys. Res. Solid Earth (1978-2012) 106 (B6), 11127–11136.

Perrin, C., Manighetti, I., Ampuero, J.P., Cappa, F., Gaudemer, Y., 2016. Location of largest earthquake slip and fast rupture controlled by along-strike change in fault structural maturity due to fault growth. J. Geophys. Res. Solid Earth 121, 2.

Romanowicz, B., 1992. Strike-slip earthquakes on quasi-vertical transcurrent faults: Inferences for general scaling relations. Geophys. Res. Lett. 19 (5), 481–484.

Romanowicz, B., Ruff, L., 2002. On moment-length scaling of large strike slip earthquakes and the strength of faults. Geophys. Res. Lett. 29 (12).

Sambridge, M., 1999. Geophysical inversion with a neighbourhood algorithm — I. Searching a parameter space. Geophys. J. Int 138, 479–494.

Scholz, C.H., 1982. Scaling laws for large earthquakes: consequences for physical models. Bull. Seismol. Soc. Am. 72 (1), 1–14.

Shaw, B.E., Scholz, C.H., 2001. Slip-length scaling in large earthquakes: observations and theory and implications for earthquake physics. Geophys. Res. Lett. 28 (15), 2995–2998.

Simmons, N.A., Myers, S.C., Johannesson, G., Matzel, E., 2012. LLNL-g3dv3: global p wave tomography model for improved regional and teleseismic travel time prediction. J. Geophys. Res. Solid Earth 117 (B10).

Sudhaus, H., Jónsson, S., 2011. Source model for the 1997 Zirkuh earthquake (mw = 7.2) in Iran derived from JERS and ERS inSAR observations. Geophys. J. Int. 185 (2), 676–692.

Takeuchi, N., 2012. Detection of ridge-like structures in the Pacific large low-shear-velocity province. Earth Planet. Sci. Lett. 319, 55–64.

Tan, Y., Helmberger, D., 2010. Rupture directivity characteristics of the 2003 Big Bear Sequence. Bull. Seismol. Soc. Am. 100 (3), 1089–1106.

Templeton, E.L., Rice, J.R., 2008. Off-fault plasticity and earthquake rupture dynamics: 1. Dry materials or neglect of fluid pressure changes. J. Geophys. Res. Solid Earth 113 (B9).

Uchide, T., Shearer, P.M., Imanishi, K., 2014. Stress drop variations among small earthquakes before the 2011 Tohoku-oki, Japan, earthquake and implications for the main shock. J. Geophys. Res. Solid Earth 119 (9), 7164–7174.

Vallée, M., 2013. Source time function properties indicate a strain drop independent of earthquake depth and magnitude. Nat. Commun. 4.

Vallée, M., Charléty, J., Ferreira, A.M., Delouis, B., Vergoz, J., 2011. SCARDEC: a new technique for the rapid determination of seismic moment magnitude, focal mechanism and source time functions for large earthquakes using body-wave deconvolution. Geophys. J. Int. 184 (1), 338–358.

Vallée, M., Douet, V., 2016. A new database of source time functions (STFs) extracted from the SCARDEC method. Phys. Earth Planet. In.

Vallée, M., Dunham, E.M., 2012. Observation of far-field mach waves generated by the 2001 Kokoxili supershear earthquake. Geophys. Res. Lett. 39 (5).

Wang, D., Mori, J., Koketsu, K., 2016. Fast rupture propagation for large strike-slip earthquakes. Earth Planet. Sci. Lett. 440, 115–126.

Wang, E., Rubin, A.M., 2011. Rupture directivity of microearthquakes on the San Andreas Fault from spectral ratio inversion. Geophys. J. Int. 186 (2), 852–866.

Warren, L.M., Shearer, P.M., 2006. Systematic determination of earthquake rupture directivity and fault planes from analysis of long-period p-wave spectra. Geophys. J. Int. 164 (1), 46–62.

Yagi, Y., 2004. Source rupture process of the 2003 Tokachi-oki earthquake determined by joint inversion of teleseismic body wave and strong ground motion data. Earth Planets Space 56 (3), 311–316.

Yue, H., Lay, T., Freymueller, J.T., Ding, K., Rivera, L., Ruppert, N.A., Koper, K.D., 2013. Supershear rupture of the 5 January 2013 Craig, Alaska (Mw 7.5) earthquake. J. Geophys. Res. Solid Earth 118 (11), 5903–5919.

Event	z (km)	M_w	(strike, dip, rake) (°)	V_r (min, max) (m/s)	T (min, max) (s)	Rupture propagation (min, max) (°)	Asymmetry (min, max)	m	r	m_{weight}	r_{weight}
19930608 NEAR EAST COAST OF KAMCHATKA	52	7.5	(228, 30, 97)	1866 (1395, 2255)	44.1 (41.0, 45.4)	157 (132, 179)	0.5 (0.4, 0.5)	0.38	0.74	0.39	0.64
19941004 KURIL ISLANDS	46	8.4	(194, 20, 48)	2274 (1634, 2886)	59.3 (56.2, 60.9)	-26 (-50, -12)	0.3 (0.2, 0.4)	0.36	0.80	0.35	0.67
19941009 KURIL ISLANDS	34	7.2	(246, 29, 120)	2271 (1616, 2781)	17.8 (16.8, 18.4)	-24 (-45, -5)	0.4 (0.4, 0.5)	0.37	0.82	0.33	0.76
19941228 OFF EAST COAST OF HONSHU JAPAN	27	7.7	(176, 15, 64)	3718 (3016, 4010)	53.6 (50.8, 54.9)	-98 (-104, -87)	0.6 (0.5, 0.7)	0.41	0.60	0.41	0.51
19950730 NEAR COAST OF NORTHERN CHILE	23	8.1	(3, 23, 103)	2851 (2566, 3563)	69.9 (68.2, 72.5)	153 (135, 163)	0.3 (0.3, 0.4)	0.24	0.59	0.27	0.48
19951009 NEAR COAST OF JALISCO MEXICO	15	7.9	(311, 22, 102)	2187 (1886, 2446)	87.5 (83.4, 87.9)	-18 (-20, 18)	0.3 (0.3, 0.3)	0.29	0.77	0.29	0.66
19951019 RYUKYU ISLANDS JAPAN	27	6.4	(38, 8, -85)	2060 (1502, 2344)	13.1 (12.5, 13.6)	-74 (-103, -67)	0.5 (0.4, 0.5)	0.37	0.82	0.31	0.71
19951203 KURIL ISLANDS	21	7.9	(239, 20, 118)	2110 (1791, 2423)	55.7 (53.6, 56.7)	180 (155, 180)	0.6 (0.6, 0.6)	0.22	0.61	0.24	0.48
19960203 YUNNAN CHINA	12	6.6	(7, 40, -59)	2680 (2242, 3530)	20.1 (19.5, 21.6)	159 (148, 177)	0.5 (0.4, 0.5)	0.45	0.81	0.49	0.73
19960217 IRIAN JAYA REGION INDONESIA	12	8.2	(85, 13, 43)	2561 (1862, 2907)	50.5 (49.1, 54.4)	180 (169, 180)	0.5 (0.4, 0.6)	0.41	0.72	0.46	0.67
19960225 OFF COAST OF GUERRERO MEXICO	12	7.1	(300, 21, 102)	1669 (1129, 2021)	16.4 (15.7, 17.3)	131 (105, 154)	0.6 (0.5, 0.7)	0.36	0.80	0.40	0.72
19960722 MINAHASSA PENINSULA SULAWESI	37	6.9	(259, 72, 91)	1633 (1402, 2072)	20.6 (20.1, 21.6)	172 (136, 180)	0.5 (0.4, 0.5)	0.31	0.87	0.31	0.79
19960723 SOUTH OF FIJI ISLANDS	8	6.5	(290, 50, -43)	4130 (2517, 4496)	21.6 (20.1, 22.7)	177 (151, 180)	0.4 (0.4, 0.5)	0.52	0.70	0.59	0.64
19961112 NEAR COAST OF PERU	26	7.8	(312, 31, 60)	2491 (2085, 3027)	55.9 (53.8, 60.7)	-160 (-175, -144)	0.8 (0.7, 0.9)	0.28	0.67	0.33	0.62
19970111 MICHOACAN MEXICO	40	7.1	(290, 85, -107)	1750 (1103, 2538)	23.4 (21.9, 24.8)	-163 (-180, -127)	0.4 (0.3, 0.4)	0.33	0.80	0.35	0.69
19970227 PAKISTAN	13	7.0	(323, 20, 138)	2602 (2107, 3495)	22.0 (20.3, 22.9)	150 (142, 179)	0.6 (0.5, 0.6)	0.41	0.77	0.45	0.64
19970421 SANTA CRUZ ISLANDS	52	7.8	(178, 67, 120)	2245 (1568, 3096)	71.5 (64.6, 74.2)	7 (-12, 41)	0.5 (0.3, 0.5)	0.45	0.78	0.48	0.67
19970510 NORTHERN AND CENTRAL IRAN	19	7.3	(162, 73, 175)	3162 (2867, 3606)	40.0 (37.4, 41.8)	-5 (-15, 0)	0.7 (0.6, 0.8)	0.44	0.67	0.48	0.61
19970706 NEAR COAST OF CENTRAL CHILE	10	6.9	(9, 22, 103)	2126 (1756, 2385)	17.6 (18.1, 19.1)	36 (-9, 36)	0.5 (0.4, 0.5)	0.43	0.79	0.41	0.70
19971205 NEAR EAST COAST OF KAMCHATKA	30	7.9	(35, 71, 90)	2412 (1863, 3192)	64.1 (61.4, 67.1)	-166 (-180, -135)	0.4 (0.3, 0.4)	0.32	0.70	0.37	0.68
19980325 BALLENY ISLANDS REGION	12	8.3	(90, 71, -28)	2480 (1745, 3507)	139.5 (132.3, 147.7)	-180 (-180, 194)	0.1 (0.1, 0.2)	0.33	0.84	0.33	0.74
19990119 NEW IRELAND REGION P.N.G.	76	7.1	(324, 55, 92)	3892 (3845, 4295)	22.5 (22.4, 24.2)	170 (170, 180)	0.5 (0.4, 0.5)	0.43	0.67	0.48	0.55
19990304 CELEBES SEA	12	7.0	(336, 39, 71)	1938 (1428, 2388)	21.7 (20.5, 22.6)	173 (152, 191)	0.7 (0.6, 0.7)	0.31	0.72	0.41	0.75
19990711 HONDURAS	5	6.7	(75, 80, 11)	2864 (2645, 3203)	16.8 (16.0, 17.3)	-163 (-166, -156)	0.4 (0.4, 0.4)	0.43	0.69	0.34	0.49
19990930 OAXACA MEXICO	43	7.4	(116, 36, -95)	2417 (2140, 3440)	22.4 (20.4, 22.6)	156 (134, 179)	0.5 (0.4, 0.5)	0.36	0.75	0.36	0.63
19991117 NEW BRITAIN REGION P.N.G.	46	7.0	(106, 53, 90)	3389 (2588, 3969)	19.0 (17.9, 20.0)	-34 (-62, -21)	0.6 (0.5, 0.7)	0.42	0.68	0.58	0.66
19991126 VANUATU ISLANDS	13	7.5	(180, 25, 90)	1518 (1252, 1886)	54.2 (52.1, 56.4)	-152 (-174, -126)	0.7 (0.6, 0.8)	0.27	0.74	0.27	0.74
20001117 NEW BRITAIN REGION P.N.G.	51	7.9	(264, 30, 87)	4067 (2841, 4982)	38.2 (36.4, 41.4)	-142 (-162, -127)	0.4 (0.3, 0.4)	0.39	0.73	0.43	0.70
20010110 KODIAK ISLAND REGION ALASKA	26	6.9	(231, 16, 78)	1741 (1348, 2450)	23.0 (22.3, 23.0)	-61 (-76, -17)	0.5 (0.4, 0.6)	0.37	0.83	0.41	0.79
20010116 SOUTHERN SUMATRA INDONESIA	34	6.8	(304, 18, 93)	2125 (1623, 2477)	16.4 (15.5, 16.9)	114 (105, 132)	0.5 (0.4, 0.5)	0.51	0.86	0.56	0.78
20010623 NEAR COAST OF PERU	33	8.4	(163, 68, 103)	2209 (1812, 2631)	99.2 (90.7, 105.3)	-5 (-33, 30)	0.7 (0.6, 0.9)	0.31	0.70	0.35	0.62
20010821 EAST OF NORTH ISLAND N.Z.	50	7.2	(206, 49, 72)	1735 (1440, 1913)	25.4 (23.2, 25.7)	39 (33, 76)	0.6 (0.6, 0.7)	0.38	0.78	0.40	0.71
20011114 QINGHAI CHINA	21	7.9	(96, 74, -8)	3406 (3097, 3671)	116.5 (107.4, 121.7)	-1 (-5, 3)	0.6 (0.6, 0.7)	0.47	0.53	0.50	0.41
20011212 SOUTH OF AUSTRALIA	18	7.1	(172, 65, 12)	2628 (2112, 3017)	24.1 (21.6, 23.9)	175 (162, 187)	0.4 (0.4, 0.5)	0.46	0.82	0.36	0.67
20021103 CENTRAL ALASKA	25	7.9	(119, 70, -162)	3458 (3254, 3769)	81.3 (76.0, 85.9)	-1 (-7, 6)	0.7 (0.6, 0.7)	0.37	0.36	0.51	0.38
20030501 TURKEY	7	6.4	(330, 82, 173)	2542 (1878, 2807)	12.4 (11.1, 12.5)	-165 (-165, -131)	0.5 (0.5, 0.6)	0.40	0.86	0.34	0.73
20030526 HALMAHERA INDONESIA	36	6.9	(321, 33, 60)	2405 (2070, 2991)	16.0 (14.7, 16.5)	-28 (-33, 3)	0.6 (0.5, 0.6)	0.39	0.67	0.44	0.61
20030715 CARLSBERG RIDGE	22	7.6	(43, 77, -150)	4254 (3659, 5064)	63.1 (57.6, 72.2)	-0 (-6, 6)	0.8 (0.6, 1.0)	0.53	0.52	0.52	0.44
20030921 MYANMAR	15	6.6	(9, 81, -174)	2123 (1538, 2355)	15.1 (14.1, 15.2)	-5 (-13, 1)	0.6 (0.6, 0.7)	0.48	0.84	0.39	0.68
20030925 HOKKAIDO JAPAN REGION	43	8.1	(253, 20, 130)	3420 (2613, 3922)	55.3 (53.1, 58.8)	-65 (-85, -40)	0.4 (0.3, 0.4)	0.38	0.74	0.39	0.73
20041122 OFF W. COAST OF S. ISLAND N.Z.	36	7.1	(46, 41, 109)	4494 (3795, 5093)	14.8 (14.0, 15.6)	-8 (-17, 7)	0.5 (0.5, 0.6)	0.47	0.71	0.51	0.64
20041223 NORTH OF MACQUARIE ISLAND	31	8.1	(246, 89, -169)	2236 (1827, 2650)	43.8 (43.8, 51.2)	17 (7, 41)	0.4 (0.3, 0.4)	0.41	0.76	0.42	0.72
20050328 NORTHERN SUMATRA INDONESIA	23	8.5	(133, 77, 90)	1320 (867, 1545)	95.9 (89.9, 97.1)	-12 (-39, 19)	0.4 (0.4, 0.5)	0.33	0.86	0.34	0.78
20050519 NORTHERN SUMATRA INDONESIA	26	6.8	(134, 73, 91)	1973 (1479, 2557)	28.5 (26.3, 29.7)	160 (143, 180)	0.3 (0.2, 0.4)	0.39	0.81	0.39	0.76
20050909 NEW IRELAND REGION P.N.G.	78	7.7	(139, 32, 89)	3350 (3140, 3802)	59.6 (57.9, 61.9)	-14 (-26, -1)	0.5 (0.4, 0.5)	0.25	0.37	0.26	0.28
20060717 SOUTH OF JAVA INDONESIA	20	7.8	(280, 13, 83)	1634 (833, 2315)	185.1 (179.9, 194.4)	109 (74, 144)	0.4 (0.3, 0.4)	0.44	0.88	0.46	0.79
20070401 SOLOMON ISLANDS	16	8.1	(305, 30, 66)	2376 (1852, 2836)	98.7 (92.5, 102.6)	-4 (-32, 15)	0.5 (0.4, 0.5)	0.36	0.72	0.35	0.62
20070624 SOUTHERN MID-ATLANTIC RIDGE	7	6.6	(261, 86, 11)	2657 (1838, 2973)	22.3 (21.5, 24.6)	-152 (-167, -132)	0.6 (0.3, 0.6)	0.35	0.74	0.34	0.64
20070802 ANDREANOF ISLANDS ALEUTIAN IS.	30	6.8	(67, 60, 80)	2460 (1936, 2847)	18.5 (17.1, 19.2)	-35 (-53, -22)	0.4 (0.4, 0.5)	0.39	0.67	0.41	0.59
20070912 SOUTHERN SUMATRA INDONESIA	21	8.4	(335, 17, 117)	2018 (1736, 2193)	107.1 (103.4, 108.1)	4 (-5, 25)	0.5 (0.5, 0.5)	0.24	0.57	0.23	0.48
20070920 SOUTHERN SUMATRA INDONESIA	33	6.7	(310, 22, 95)	1647 (1155, 2050)	15.1 (14.5, 16.2)	86 (66, 103)	0.5 (0.4, 0.6)	0.37	0.88	0.36	0.79
20071107 NORTH OF MACQUARIE ISLAND	23	6.6	(217, 71, 168)	4076 (3596, 4351)	24.3 (22.8, 25.9)	178 (164, 180)	0.3 (0.3, 0.4)	0.47	0.65	0.46	0.53
20071114 NORTHERN CHILE	47	7.8	(354, 25, 97)	2462 (2007, 3090)	52.6 (49.0, 53.9)	165 (140, 178)	0.4 (0.4, 0.5)	0.41	0.79	0.40	0.66
20080329 OFF W COAST OF NORTHERN SUMATRA	24	6.4	(320, 10, 98)	2018 (1656, 2673)	13.0 (12.3, 13.7)	-79 (-80, -44)	0.6 (0.6, 0.7)	0.42	0.84	0.44	0.77
20090103 IRIAN JAYA REGION INDONESIA	13	7.6	(109, 27, 66)	1591 (1266, 2282)	32.9 (29.8, 33.6)	-15 (-45, 17)	0.3 (0.3, 0.4)	0.36	0.86	0.37	0.73
20090528 NORTH OF HONDURAS	24	7.4	(67, 79, -7)	4105 (3286, 5371)	55.2 (48.3, 57.0)	-155 (-155, 218)	0.1 (0.0, 0.2)	0.40	0.77	0.44	0.64
20090715 OFF W. COAST OF S. ISLAND N.Z.	28	7.7	(33, 33, 143)	2547 (1805, 3178)	27.0 (26.1, 28.8)	138 (109, 151)	0.5 (0.4, 0.6)	0.42	0.80	0.47	0.74
20090810 ANDAMAN ISLANDS INDIA REGION	12	7.7	(191, 17, -124)	1842 (1331, 2200)	42.9 (41.3, 44.1)	-137 (-176, -130)	0.6 (0.6, 0.7)	0.40	0.84	0.38	0.78
20090816 SOUTHERN SUMATRA INDONESIA	16	6.8	(168, 30, 96)	2758 (2289, 3531)	15.8 (15.4, 17.0)	79 (67, 95)	0.4 (0.4, 0.5)	0.42	0.84	0.40	0.73
20091209 CENTRAL MID-ATLANTIC RIDGE	11	6.5	(78, 82, 172)	1397 (1209, 2332)	25.9 (24.0, 28.0)	9 (-35, 19)	0.4 (0.4, 0.5)	0.48	0.84	0.45	0.78
20100103 SOLOMON ISLANDS	12	7.1	(325, 16, 109)	1215 (1123, 2160)	23.9 (22.5, 26.0)	2 (-35, 11)	0.6 (0.5, 0.7)	0.40	0.85	0.36	0.75
20100227 NEAR COAST OF CENTRAL CHILE	20	8.8	(176, 72, 80)	1841 (1437, 2411)	117.5 (111.8, 122.9)	-180 (-180, -138)	0.5 (0.4, 0.5)	0.40	0.77	0.47	0.74
20100406 NORTHERN SUMATRA INDONESIA	19	7.8	(306, 15, 84)	1820 (1435, 2235)	40.3 (38.6, 42.0)	92 (70, 108)	0.6 (0.5, 0.7)	0.37	0.78	0.35	0.67
20100413 QINGHAI CHINA	16	6.9	(120, 85, -5)	2119 (1556, 2535)	19.3 (17.4, 20.0)	23 (-21, 34)	0.5 (0.5, 0.6)	0.44	0.81	0.38	0.62
20100505 SOUTHERN SUMATRA INDONESIA	27	6.5	(310, 14, 92)	1912 (1676, 2362)	16.6 (15.2, 16.8)	-12 (-38, -6)	0.5 (0.5, 0.6)	0.44	0.82	0.50	0.78
20100509 NORTHERN SUMATRA INDONESIA	36	7.2	(303, 19, 83)	2287 (1423, 2680)	21.2 (20.4, 22.6)	98 (65, 112)	0.5 (0.4, 0.5)	0.39	0.81	0.44	0.77
20100612 NICOBAR ISLANDS INDIA REGION	31	7.4	(227, 46, 47)	3425 (2691, 4456)	29.7 (27.4, 32.3)	172 (161, 180)	0.4 (0.3, 0.5)	0.51	0.87	0.48	0.76
20100616 IRIAN JAYA REGION INDONESIA	13	7.0	(336, 65, -162)	3187 (2617, 3862)	24.1 (22.4, 26.7)	-2 (-15, 9)	0.4 (0.3, 0.5)	0.51	0.76	0.49	0.68
20101025 SOUTHERN SUMATRA INDONESIA	12	7.9	(320, 8, 95)	1948 (1344, 2257)	88.4 (84.3, 91.2)	41 (18, 55)	0.3 (0.3, 0.4)	0.31	0.75	0.30	0.67
20110126 NORTHERN SUMATRA INDONESIA	24	6.1	(321, 15, 97)	1670 (1041, 2059)	11.9 (11.3, 12.4)	152 (140, 174)	0.7 (0.6, 0.7)	0.34	0.79	0.33	0.67
20110211 NEAR COAST OF CENTRAL CHILE	28	6.8	(2, 20, 97)	1615 (1303, 1962)	19.7 (19.0, 20.6)	-8 (-31, 21)	0.5 (0.4, 0.5)	0.38	0.78	0.40	0.75
20110322 OFF EAST COAST OF HONSHU JAPAN	9	6.4	(210, 43, -104)	2852 (2152, 3783)	7.6 (6.9, 8.5)	14 (-13, 35)	0.8 (0.7, 1.0)	0.53	0.83	0.59	0.76
20110706 KERMADEC ISLANDS REGION	16	7.6	(15, 43, -72)	2101 (1549, 2665)	27.5 (26.8, 29.7)	-15 (-55, 0)	0.4 (0.3, 0.4)	0.35	0.84	0.38	0.79
20110916 NEAR EAST COAST OF HONSHU JAPAN	24	6.8	(201, 15, 86)	2611 (2218, 2881)	19.0 (18.4, 20.1)	95 (82, 101)	0.8 (0.7, 0.8)	0.27	0.65	0.33	0.58
20111021 KERMADEC ISLANDS REGION	47	7.4	(198, 39, 80)	3992 (3492, 5301)	18.2 (17.4, 19.7)	148 (123, 173)	0.4 (0.3, 0.5)	0.48	0.74	0.49	0.64
20120110 OFF W COAST OF NORTHERN SUMATRA	12	7.2	(190, 79, -12)	1828 (1371, 2093)	33.7 (31.3, 35.5)	180 (174, 180)	0.2 (0.2, 0.2)	0.38	0.85	0.27	0.72
20120830 JAN MAYEN ISLAND REGION	14	6.8	(109, 75, 0)	3183 (3014, 3724)	21.9 (20.4, 23.2)	-8 (-14, 8)	0.6 (0.5, 0.7)	0.48	0.63	0.42	0.49
20121111 MYANMAR	20	6.9	(1, 66, 194)	2527 (2004, 3094)	24.2 (22.3, 25.8)	172 (158, 180)	0.6 (0.5, 0.7)	0.39	0.79	0.31	0.68
20130201 SANTA CRUZ ISLANDS	21	6.4	(305, 20, 64)	3374 (3039, 3818)	14.3 (12.7, 14.0)	79 (47, 79)	0.5 (0.5, 0.6)	0.41	0.67	0.46	0.65
20130228 KURIL ISLANDS	45	6.9	(49, 58, 90)	2436 (1500, 2945)	19.1 (17.7, 20.2)	-22 (-47, -6)	0.4 (0.3, 0.4)	0.47	0.84	0.51	0.77
20130419 KURIL ISLANDS	109	7.2	(120, 8, -33)	2279 (1863, 2667)	24.6 (24.2, 26.6)	-73 (-99, -69)	0.6 (0.5, 0.7)	0.39	0.67	0.37	0.58
20131019 GULF OF CALIFORNIA	8	6.6	(131, 79, 178)	1532 (1166, 2508)	13.7 (13.5, 14.8)	168 (143, 179)	0.7 (0.5, 0.7)	0.48	0.90	0.43	0.77
20131024 EAST OF SOUTH SANDWICH ISLANDS	29	6.7	(81, 89, 9)	3129 (2710, 3649)	27.1 (25.4, 29.7)	-166 (-180, -142)	0.6 (0.5, 0.7)	0.37	0.50	0.30	0.37
20131031 NEAR COAST OF CENTRAL CHILE	33	6.5	(350, 33, 90)	2748 (2024, 3083)	7.6 (6.9, 8.1)	-154 (-177, -142)	0.8 (0.8, 1.0)	0.48	0.75	0.47	0.71
20131117 SCOTIA SEA	34	7.8	(96, 61, -11)	1670 (1106, 2850)	129.3 (121.1, 138.6)	6 (-59, 35)	0.2 (0.1, 0.3)	0.38	0.89	0.34	0.76
20131125 FALKLAND ISLANDS REGION	16	7.0	(70, 77, 12)	3406 (2937, 4182)	25.9 (23.7, 28.9)	-7 (-11, 19)	0.3 (0.2, 0.5)	0.38	0.77	0.43	0.65
20140418 GUERRERO MEXICO	20	7.3	(300, 20, 91)	2151 (1363, 2800)	32.0 (30.5, 33.4)	12 (-12, 42)	0.2 (0.2, 0.3)	0.38	0.83	0.38	0.77
20140524 AEGEAN SEA	12	7.0	(73, 79, 180)	1899 (1383, 2183)	37.6 (35.3, 38.9)	6 (3, 34)	0.5 (0.4, 0.5)	0.31	0.71	0.30	0.64
20140623 RAT ISLANDS ALEUTIAN ISLANDS	116	7.9	(214, 28, -5)	1557 (1030, 1973)	37.7 (37.0, 40.2)	-28 (-44, -6)	0.6 (0.4, 0.6)	0.33	0.79	0.38	0.78
20141014 OFF COAST OF CENTRAL AMERICA	54	7.2	(131, 17, -90)	3683 (2945, 4268)	18.1 (17.3, 20.1)	-76 (-86, -54)	0.4 (0.3, 0.4)	0.50	0.76	0.48	0.73
20150329 NEW BRITAIN REGION P.N.G.	43	7.6	(258, 29, 90)	3177 (2028, 3369)	29.8 (28.7, 32.0)	89 (84, 108)	0.6 (0.5, 0.6)	0.40	0.82	0.47	0.80
20150425 NEPAL	12	7.9	(102, 83, 88)	3026 (2796, 3358)	47.3 (46.2, 48.8)	15 (6, 29)	0.5 (0.5, 0.6)	0.30	0.43	0.30	0.36
20150505 NEW BRITAIN REGION P.N.G.	47	7.5	(79, 63, 90)	2827 (2212, 3853)	38.8 (37.7, 43.1)	21 (-13, 36)	0.4 (0.3, 0.5)	0.40	0.77	0.46	0.73
20151108 NICOBAR ISLANDS INDIA REGION	17	6.9	(322, 90, -177)	2469 (1916, 3493)	18.9 (17.9, 20.3)	180 (141, 237)	0.4 (0.4, 0.5)	0.45	0.73	0.45	0.63
20151111 OFF COAST OF CENTRAL CHILE	16	6.9	(33, 20, 125)	2208 (1474, 2750)	19.4 (17.8, 20.1)	-2 (-19, 29)	0.4 (0.4, 0.5)	0.42	0.80	0.46	0.75
20151204 SOUTHEAST INDIAN RIDGE	20	7.1	(178, 53, -122)	2634 (1750, 3782)	24.2 (23.1, 26.0)	16 (-10, 47)	0.3 (0.2, 0.3)	0.47	0.83	0.46	0.73

Table S1: List of the 96 earthquakes from our rupture catalog. The four main rupture parameters are reported here, with their respective uncertainties : rupture velocity V_r, rupture propagation angle ξ, asymmetry ratio x_{fm}. m, r, m_{weight}, r_{weight} correspond respectively to the misfit, the ratio of misfit to a point source model misfit, and their corresponding values when stations are weighted. Focal depth (z), moment magnitude (M_w) and focal mechanism come from the SCARDEC database.